International Journal of Minerals, Metallurgy and Materials
Accepted manuscript, https://doi.org/10.1007/s12613-024-3003-8

Robust interface and excellent as-built mechanical properties of Ti–6Al–4V fabricated through laser aided additive manufacturing with powder and wire

Fei Weng[1,3)], *Guijun Bi*[2,3),✉], *Youxiang Chew*[3),✉], *Shang Sui*[3)], *Chaolin Tan*[3)], *Zhenglin Du*[3)], *Jinlong Su*[3)], *and Fern Lan Ng*[3)]

1) Key Laboratory for Liquid-Solid Structural Evolution and Processing of Materials, Ministry of Education, Shandong Engineering & Technology Research Center for Superhard Material, School of Materials Science and Engineering, Shandong University, Jinan 250061, China

2) Institute of Intelligent Manufacturing, Guangdong Academy of Sciences, Guangzhou 510095, China

3) Singapore Institute of Manufacturing Technology, 5 Cleantech Loop, 636732, Singapore

✉Corresponding authors: Guijun Bi E-mail: gj.bi@giim.ac.cn; Youxiang Chew E-mail: chewyx@simtech.a-star.edu.sg

(Received: 25 June 2024; revised: 15 August 2024; accepted: 9 September 2024)

Abstract:

The feasibility of manufacturing Ti–6Al–4V samples through a combination of laser-aided additive manufacturing with powder ($LAAM_p$) and wire ($LAAM_w$) was explored. A process study was first conducted to successfully circumvent defects in Ti–6Al–4V deposits for $LAAM_p$ and $LAAM_w$, respectively. With the optimized process parameters, robust interfaces were achieved between powder/wire deposits and the forged substrate, as well as between powder and wire deposits. Microstructure characterization results revealed the epitaxial prior β grains in the deposited Ti–6Al–4V, wherein the powder deposit was dominated by a finer α′ microstructure and the wire deposit was characterized by lamellar α phases. The mechanisms of microstructure formation and correlation with mechanical behavior were analyzed and discussed. The mechanical properties of the interfacial samples can meet the requirements of the relevant Aerospace Material Specifications (AMS 6932) even without post heat treatment. No fracture occurred within the interfacial area, further suggesting the robust interface. The findings of this study highlighted the feasibility of combining $LAAM_p$ and $LAAM_w$ in the direct manufacturing of Ti–6Al–4V parts in accordance with the required dimensional resolution and deposition rate, together with sound strength and ductility balance in the as-built condition.

Keywords: laser-aided additive manufacturing; powder deposition; wire deposition; interfacial characteristic; mechanical behavior

1. Introduction

Titanium alloys are widely used in the aerospace, biomedical, and chemical industries owing to their outstanding mechanical performance, biocompatibility, and corrosion resistance [1]. In recent

decades, additive manufacturing (AM) technology has been developed substantially, drawing great attention from the industry and academia [2–6], with studies on the AM of titanium alloys being extensively reported [7–9]. The primary research emphasis is tailoring microstructures for a balance of strength and ductility [9–10].

An advantage of AM technology, especially directed energy deposition (DED) techniques, such as laser aided additive manufacturing (LAAM) with powder or wire [11–14], is fabricating add-on features on existing parts or repairing high-value components. Existing parts or components can be processed through conventional manufacturing or AM techniques. For example, Liu *et al.* [15] fabricated TiAl blades on a Ti–6Al–4V cylinder by using laser AM with powder delivery. Similarly, Paydas *et al*. [16] simulated repair by filling up a pre-machined profile on a Ti–6Al–4V base plate. Shi *et al*. [17] reported a hybrid fabrication process using wire arc AM (WAAM) to fabricate add-on features on Ti–6Al–4V plates manufactured through selective laser melting (SLM). The feasibility of this hybrid AM technique was also studied in Ref. [18]. On the above-mentioned occasions, interfacial characteristics and mechanical behaviors, apart from the microstructure and properties of the bulk deposits, are of great concern. For combinations of different materials, functionally graded materials have been developed to address potential interfacial issues [19–20]. The interfacial quality and mechanical properties of the same material processed with different techniques are also of great interest to researchers and end-users.

Although some reports on the interfacial characteristics and mechanical behaviors of AM-processed and commercial titanium alloys (e.g., Ti–6Al–4V) exist, almost all are based on laser DED with powder ($LDED_p$) [21–24]. As mentioned above, wires can also be used as feedstock material in AM processes, such as laser DED with wire ($LDED_w$) [25] and WAAM [26]. $LDED_w$ has the advantages of a lower feedstock price, higher deposition and material utilization rates, and a considerably cleaner process than $LDED_p$. In principle, $LDED_w$ can also be used to fabricate add-on features on existing titanium substrates to substitute for powder deposition in the fabrication of sections with simple structures but large sizes. $LDED_p$ can be used in tandem with $LDED_w$ to achieve a balance in build efficiency and dimensional accuracy. Moreover, powder and wire delivery systems, which are interchangeable in accordance with requirements, can be integrated into the same deposition system. Although the combination of powder and wire in LDED has been reported previously, it was mainly employed to fabricate composites or functionally graded materials by using feeding powder and wire simultaneously, such as ER5356 Al alloy wire + SiC powder [27], Ti–6Al–4V wire + WC powder [28], and Ti–6Al–4V wire + TiC powder [29]. Furthermore, the coincident wire-powder feeding of the same material (e.g., 316L [30–31]) was explored, aiming at enhanced surface quality, high deposition efficiency, and performance. However, the AM of Ti–6Al–4V alloy tends to form acicular α′, which results in high strength but low elongation. Hence, post heat treatment

is necessary to tune microstructures to achieve balanced strength and ductility. However, post heat treatment of large parts is challenging and inconvenient.

Different from simultaneous wire-powder feeding, herein, we emphasize the synergy of the LAAM with powder ($LAAM_p$) and wire ($LAAM_w$) in manufacturing an integrated Ti–6Al–4V part to achieve acceptable mechanical properties in the as-built condition such that post heat treatment can be eliminated. $LAAM_p$ is more flexible and exhibits better dimensional accuracy, whereas $LAAM_w$ shows a higher deposition rate and is advantageous in processing large-size parts. The combination of $LAAM_p$ and $LAAM_w$ is expected to achieve the synergy of the two processes. As mentioned earlier, the quality of the interface between the $LAAM_p$- and $LAAM_w$-processed Ti–6Al–4V and resultant as-built mechanical properties are vital to the performance of the final part. However, the combination of $LAAM_p$ and $LAAM_w$ faces a lack of evidence for process optimization and the verification of the interface quality and mechanical behavior.

In this study, process optimization was first conducted to ensure the successful deposition of the Ti–6Al–4V powder and wire. Subsequently, samples were fabricated to evaluate the quality of the interfaces among the powder deposit, wire deposit, and forged substrate. Subsequently, the interfacial sample of the powder deposit on the wire deposit was manufactured to extract samples for microstructure and mechanical behavior evaluation. For comparison, the powder and wire deposits on the forged substrate were also fabricated. This study provides a set of optimized process parameters for manufacturing Ti–6Al–4V parts with good interface quality and mechanical properties in the as-built condition by using a combination of $LAAM_p$ and $LAAM_w$, laying a foundation for the application of $LAAM_p$, $LAAM_w$, or a combination of these techniques in fabricating add-on features on existing commercial substrates and repairing high-value components without post heat treatment.

2. Materials and methods

2.1. Materials

Commercial Ti–6Al–4V powders with a particle size of 20–53 μm (LPW technology, currently under Carpenter, the USA) and wire with a diameter of 1.0 mm (Allalloy, Singapore) were used as the feedstock materials. The powder and wire were grade 23 Ti–6Al–4V, a kind of extra low interstitial titanium alloy with better ductility and fracture toughness [32]. Forged Ti–6Al–4V was used as the substrate. The typical microstructures of the forged Ti–6Al–4V are shown in Fig. 1(a)–(f). The forged Ti–6Al–4V was mainly composed of a bimodal structure: primary granular α and lamellar α + β (transformed β). Given that the forged substrate was cut from a large Ti–6Al–4V component, the microstructure, especially the lamellar α + β, is coarser at the position further away (approx. >30 mm) from the surface of the component (Fig. 1(a)). In comparison, the section near the component surface (within approx. 30 mm) shows finer microstructure (Fig. 1(b)) owing to the high

cooling rate after forging. Fig. 1(c)–(d) provides a close-up view of the lamellar α + β. As shown in Fig. 1(e) and (f), the granular α is rich in Al, an α stabilizer in titanium alloys.

2.2. $LAAM_p$ and $LAAM_w$ setup

Fig. 2(a) and (b) depicts the LAAM system in our lab with integrated coaxial powder feeding and lateral wire delivery modules. The angle between the wire feeding tube and the horizontal plane is approximately 50°. The schematic of $LAAM_p$ and $LAAM_w$ is shown in Fig. 2(c). A continuous coaxial nozzle was used for powder feeding, wherein a central shielding gas (Ar) was used to protect the melt pool from oxidation. The central shielding gas was also applied during wire deposition with a gas pressure and flow rate of 0.1 MPa and 10 min^{-1}. An additional shielding gas tube was added for better protection of the deposit from oxidation during wire deposition at the gas pressure and flow rate of 0.1 MPa and 20 min^{-1}, respectively.

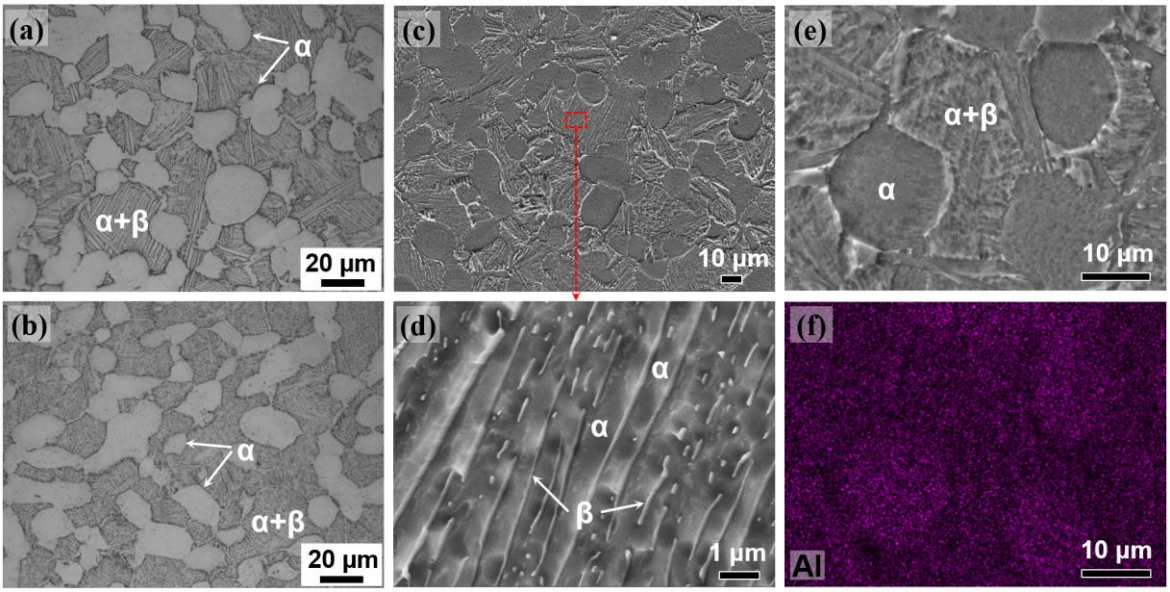

Fig. 1. Microstructure of the forged Ti–6Al–4V: (a) the sample extracted far from the surface of a large component (approx. >30 mm away from the surface). (b) the sample near the surface of a large component (approx. <30 mm away from the surface). (c, d) Close-up view of the lamellar α + β structure. (e, f) Bimodal microstructure and corresponding energy dispersive X-ray spectroscopy (EDX) mapping.

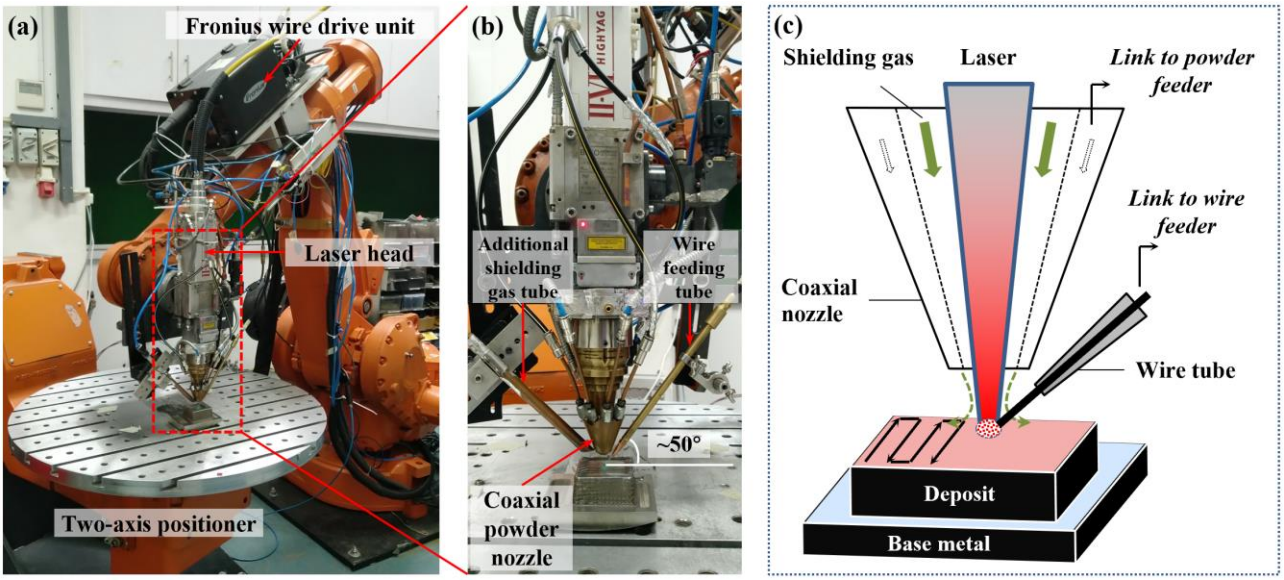

Fig. 2. (a, b) LAAM setup with coaxial powder and lateral wire feeding units. (c) Schematic of $LAAM_p$ and $LAAM_w$.

2.3. Fabrication of deposits and strategy of deposition

The main process parameters for $LAAM_p$ and $LAAM_w$ include laser power, scan velocity, beam size, hatch distance, and powder/wire feed rate. Similar to those in other AM works, the process parameters in this work were first optimized to eliminate defects, such as lack of fusion (LoF) and entrapped pores. Different from the powder deposition process, the wire is not as flexible as the powder, so the parameter window is relatively narrow. A criterion for the process optimization of $LAAM_w$ is to ensure continuous deposition, i.e., the wire fed into the melt pool is thoroughly melted and continuously deposited onto the substrate. The process parameters after the process optimization of $LAAM_p$ and $LAAM_w$ are listed in Table 1. Some of the results of process optimization are introduced in Section 3.1.

Table 1. Main process parameters for powder and wire deposition

Technique	Power, P / W	Scan velocity, v / (mm·min^{-1})	Single track width, w / mm	Area energy density, E / (J·mm^{-2})	Hatch distance, h / mm	Powder or wire feed rate	Layer thickness, ΔZ / mm
$LAAM_p$	580	800	1.7	25.6	0.85	1.37 g/min	~0.4
$LAAM_w$	1500	480	4.0	46.9	2.2	1.1 m/min	~0.9

During powder and wire deposition, the scan direction was rotated by 90° between adjacent layers. Given that the lateral wire feeding strategy was used in this study, interlayer rotation was implemented by rotating the sample by 90° (Fig. 3), which can be realized by programming the processing code, executing the rotation of the positioner in the X–Y plane by 90° after the deposition of one layer.

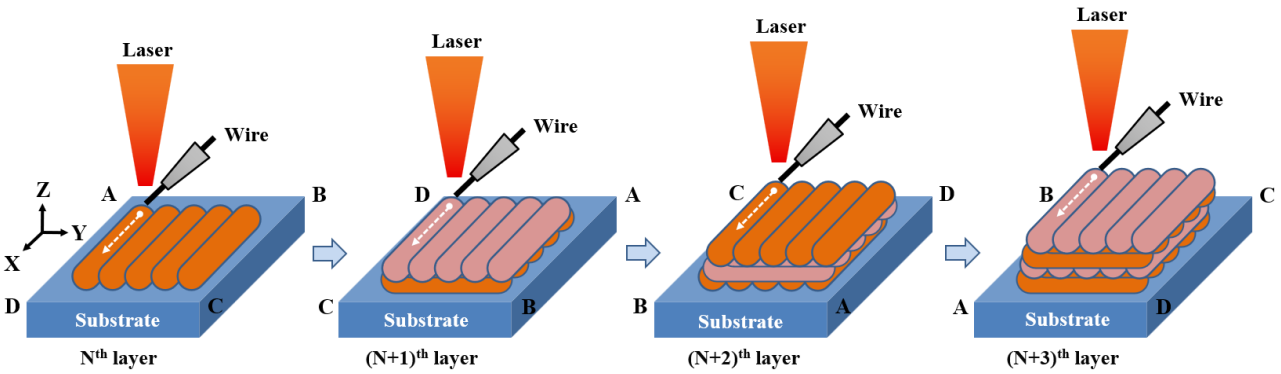

Fig. 3. Deposition strategy of $LAAM_w$.

On the basis of the optimized parameters, small interfacial samples were fabricated for the preliminary evaluation of interface quality. Subsequently, larger samples were fabricated to extract specimens for the further investigation of microstructures and interfacial mechanical behavior. Sample codes are summarized in Table 2.

Table 2. List of the sample codes

Abbreviation	Deposited sample
PD	Powder deposit
WD	Wire deposit
PW	Powder deposit on the wire deposit
PF	Powder deposit on the forged substrate
WF	Wire deposit on the forged substrate

For the PF and WF samples, the forged substrate dimension is 60 mm × 60 mm × 65 mm. The dimensions of the powder and wire deposits are 40 mm × 40 mm × 65 mm and 50 mm × 50 mm × 65 mm, respectively. For the PW sample, the wire deposit (50 mm × 50 mm × 65 mm) was first fabricated on a forged Ti–6Al–4V substrate (60 mm × 60 mm × 20 mm). Subsequently, the powder deposit with dimensions of 50 mm × 50 mm × 65 mm was deposited on top of the wire deposit.

2.4. Microstructure characterization and mechanical testing

Tensile coupons with gauge dimensions of 25 mm × 6 mm × 4 mm were extracted from a deposited block (Fig. 4) to evaluate interfacial characteristics and mechanical behavior. The tensile test was conducted on an Instron 5982 universal testing machine (Instron, the USA) by using the crosshead speed control method with a constant crosshead extension rate of 1 mm/min. The corresponding nominal strain rate was ~0.03 /min. Three samples from each group were tested, and the results were averaged to ensure reliability. The ASTM E8 standard was used as a reference for the tensile test. Tensile loading was applied along the build direction. Microhardness was tested by using an MMT-X3 digital micro Vickers hardness tester (MATSUZAWA, Japan). The load for the microhardness test was 3N.

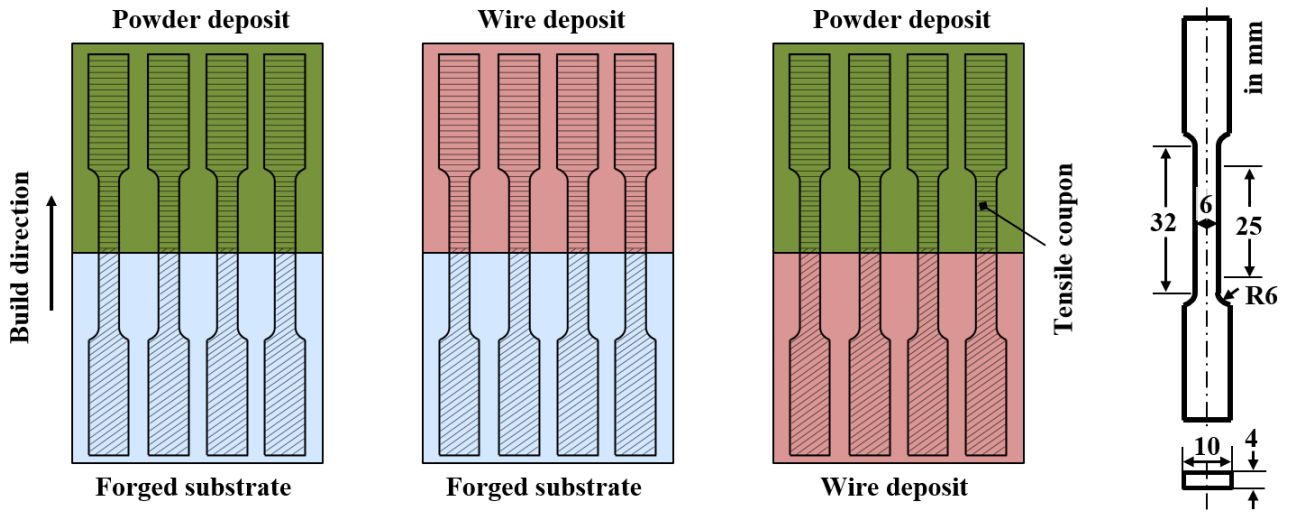

Fig. 4. Extraction of tensile coupons from interfacial samples.

Metallurgical samples were prepared by performing the steps of plane grinding, fine grinding, and polishing on MD-Mezzo 220, MD-Largo, and MD-Chemistry grinding/polishing disks, respectively. DiaPro Allegro/Largo (9 μm) was used for fine grinding, and final polishing was conducted with an oxide polishing suspension (0.25 μm). The above-mentioned grinding and polishing accessories were purchased from Struers, Denmark. The samples for microstructure observation were etched by using Kroll's reagent (HF : HNO_3 : H_2O = 2:6:92, vol%). Microstructure characteristics were observed with an MX51 optical microscope (Olympus, Japan). Electron backscatter diffraction (EBSD) analysis was conducted on an Ultra Plus scanning electron microscope (SEM, Carl Zeiss, Germany) equipped with an EBSD detector (Oxford Instruments, the UK). The acquisition step sizes were 0.25 and 0.06 μm for the low-magnification overview and high-magnification close-up observation, respectively. Fractographs were also observed by using SEM.

3. Results

3.1. Process optimization for robust interfaces

Intertrack or interlayer LoF defects are the most detrimental defects for the mechanical properties of AM-processed alloys, especially along the build direction. The tip to eliminate the LoF defects is that the laser energy input is sufficient to melt the materials fed into the melt pool, as well as to partially remelt the previously deposited material or the substrate. Fig. 5(a) and (b) depicts some typical LoF defects in the powder and wire deposits, respectively. Some unmelted powders are observed within the LoF defects (Fig. 5(a)), implying that the laser energy input was insufficient. Herein, the powder feed rate was excessively high (2.24 g/min) despite the high laser power (670 W) used. The direct route to eliminate the LoF defects is increasing the laser energy heat input (e.g., increasing the laser power) or reducing the powder/wire feed rate. Therefore, in the optimized

parameters (Table 1), a lower powder feed rate (1.37 g/min), along with a lower laser power (580 W) to prevent overheating, was used for powder deposition.

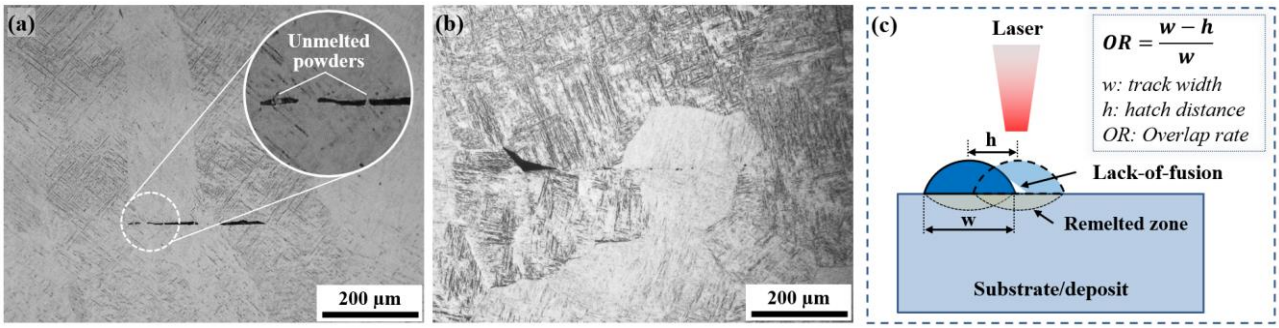

Fig. 5. (a) LoF defects in the powder deposit (P = 670 W, powder feed rate = 2.24 g/min). (b) LoF defects in the wire deposit (hatch distance = 2.0 mm). (c) Schematic of the formation of LoF defects.

Similarly, Fig. 5(b) shows typical intertrack LoF defects in the wire deposit, wherein a hatch distance of 2.0 mm was used. During LAAM, partial laser energy input is consumed to remelt the substrate or deposits, as shown in Fig. 5(c). Therefore, an excessively high overlap rate (i.e., low hatch distance) results in insufficient energy to melt the newly added material thoroughly, causing intertrack LoF defects, as shown in Fig. 5(b). Although increasing the laser power can circumvent the formation of this kind of LoF, higher laser power facilitates wire backflow, resulting in wire nozzle clogging and breaking process stability. Therefore, a larger hatch distance is helpful for eliminating intertrack LoF during LAAM$_w$. Therefore, a higher hatch distance and lower overlap rate (2.2 mm and 45%) were adopted.

With the optimized parameters (Table 1), the LoF defects were eliminated, indicating that the powder and wire deposits, when deposited separately, are defect-free. However, the interface quality between the powder and wire deposits remains unknown. Will the as-built deposit surface affect interface quality? What are the microstructure characteristics of the powder deposit, wire deposit, and interfacial zone? Will the mechanical behavior of the interfacial sample be comparable to those of the powder deposit, wire deposit, and commercially forged Ti–6Al–4V?

In consideration of the above questions, we first fabricated some small test blocks by directly performing powder deposition on the as-built surface of the wire deposit and directly conducting wire deposition on the as-built surface of the powder deposit. For example, the wire deposit was first fabricated on the forged Ti–6Al–4V substrate. After being cooled down, the powder deposit was directly deposited on the wire deposit. The deposition directions for the last layer of the wire deposit and the first layer of the powder deposit were orthogonal to each other. The cross-section overview of the small interfacial sample (Fig. 6(a) and (b)) and close-up view (Fig. 6(c) and (d)) showed that no LoF defects were present within the powder deposit, wire deposit, and interfacial zone despite the coarse as-built surface. Subsequently, the microstructure characteristics and mechanical behaviors of

the interfacial samples, as well as microstructure–property correlations, were further investigated to provide more substantial evidence for the application of versatile LAAM techniques.

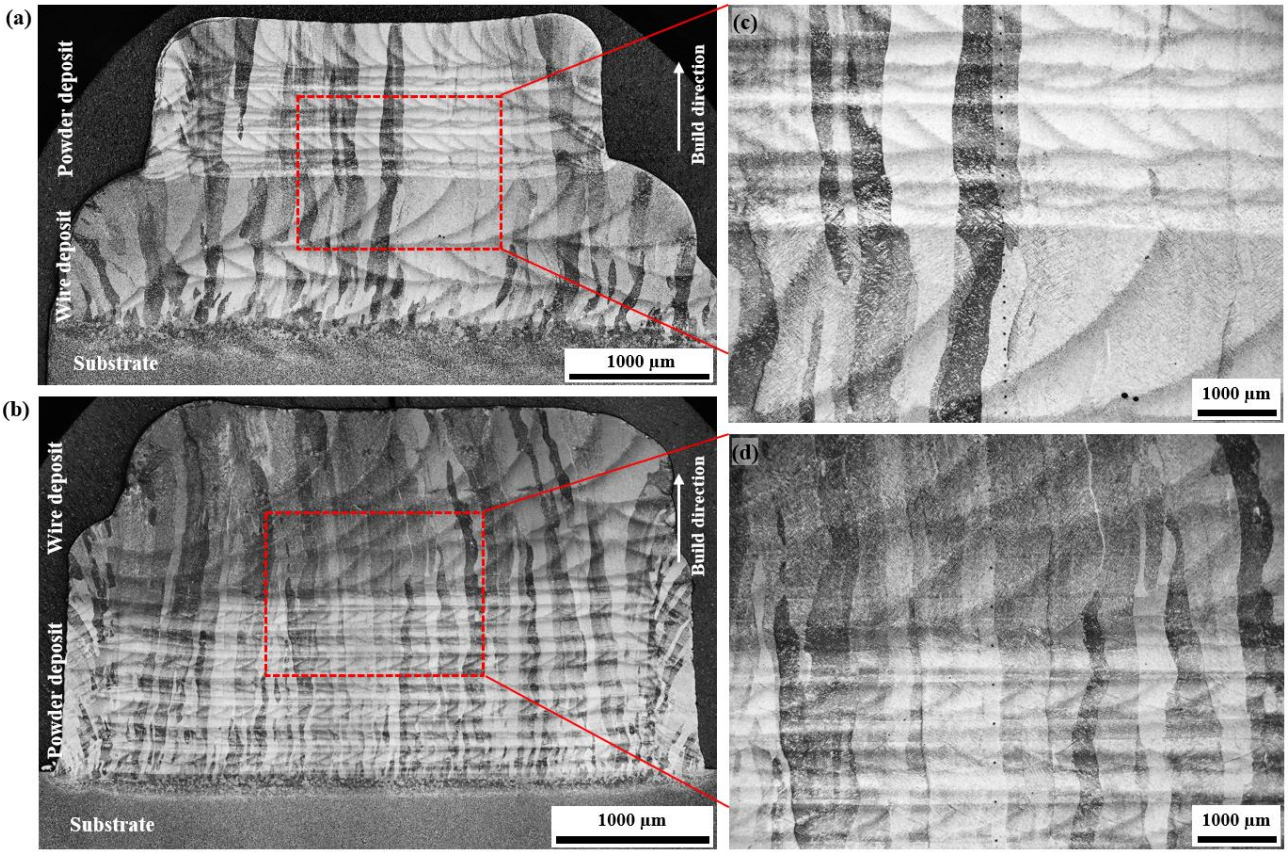

Fig. 6. Cross-section overview of the small interfacial samples: (a, c) powder deposit on the wire deposit; (b, d) wire deposit on the powder deposit.

3.2. Microstructure characteristics of the powder deposit, wire deposit, and interface

Different samples were fabricated on the basis of process optimization, as mentioned in Table 2. Herein, the PW sample (i.e., the powder deposit on the wire deposit) was chosen for the in-depth microstructure analysis of the powder deposit, wire deposit, and interface. Similar to the results in Fig. 6, the cross-section overview of the PW sample is characterized by columnar prior β grains growing along the build direction and across dozens of layers as well as the interface (Fig. 7(a)). The columnar β grains are derived from the epitaxial growth inverse to the approximately maximum heat conduction direction, which is commonly observed in additive-manufactured titanium alloys [33]. The typical microstructures in the prior β grains of the powder and wire deposits are depicted in Fig. 7(b) and (c), respectively. Owing to the high cooling rate, numerous acicular martensitic phases (α′) are formed in the powder deposit, whereas basket-weave microstructures (lamellar α phases), derived from the slower cooling rate, are observed in the wire deposit.

The EBSD analysis results of the as-built PW sample are provided in Fig. 8. Evidently, the α′ phase in the powder deposit is finer than the α phase in the wire deposit. The lath thickness was derived through the EBSD analysis of grain size by assuming each lath as an equivalent ellipse and taking the

minor axis length as the thickness [34]. The area-weighted mean value of the minor axis length was regarded as the thickness. On the basis of the EBSD data in Fig. 8(a) and (b), the α′ and α lath thicknesses are (1.1 ± 0.3) and (2.9 ± 0.9) μm, respectively. In addition, the average aspect ratio of the α′ lamellar structure (6.8 ± 2.3) is higher than that of α lamellae (4.3 ± 2.0).

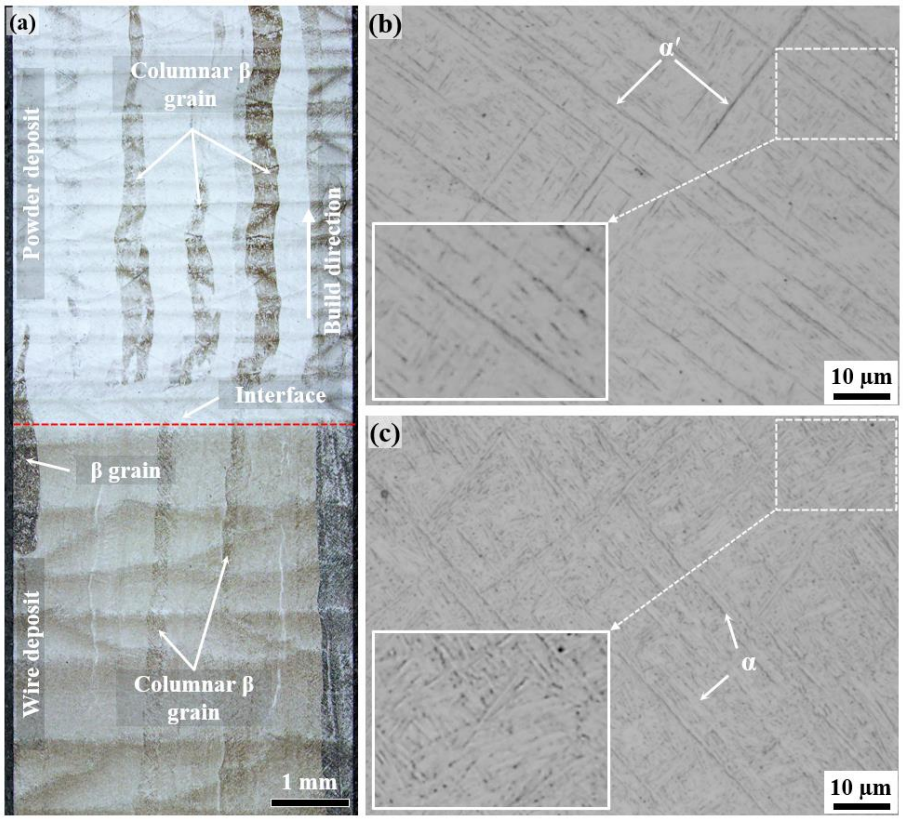

Fig. 7. (a) Cross-section overview of the powder deposit on the wire deposit (PW) sample. (b) Typical microstructure in the prior β grain of the powder deposit side. (c) Typical microstructure in the prior β grain of the wire deposit side.

The difference in the sizes and morphologies of the α′ and α phases is attributed to the different thermal histories in $LAAM_p$ and $LAAM_w$. The prior columnar β grain boundaries are outlined with white dotted lines in Fig. 8(b) and (c). Fig. 8(f)–(h) and (j)–(l) shows the elemental distribution of the typical microstructure of the powder and wire deposits, respectively. Compared with that in the powder deposit (Fig. 8(f)–(h)), elemental segregation is more evident in the wire deposit (Fig. 8(j)–(l)). During $LAAM_p$, the higher cooling rate leads to nondiffusive martensitic transformation (β → α′). However, the slight segregation that has appeared in the powder deposit (Fig. 8(g) and (h)) is due to the partial decomposition of the α′ phase [35] and is discussed later. At a lower cooling rate in $LAAM_w$, the formation of α is subject to diffusive transformation from the parent β, and elemental redistribution results in obvious Al segregation (i.e., Al rich in α and Al lean in β), as shown in Fig. 8(j). The interfacial characteristic is shown in Fig. 8(c), and the EBSD analysis position is illustrated in Fig. 9. The prior β grains growing across the powder/wire deposit interface are observed in Fig.

8(c), suggesting robust metallurgical bonding. The robust interfaces between different combinations of the deposits and forged substrate are further verified by the tensile testing results.

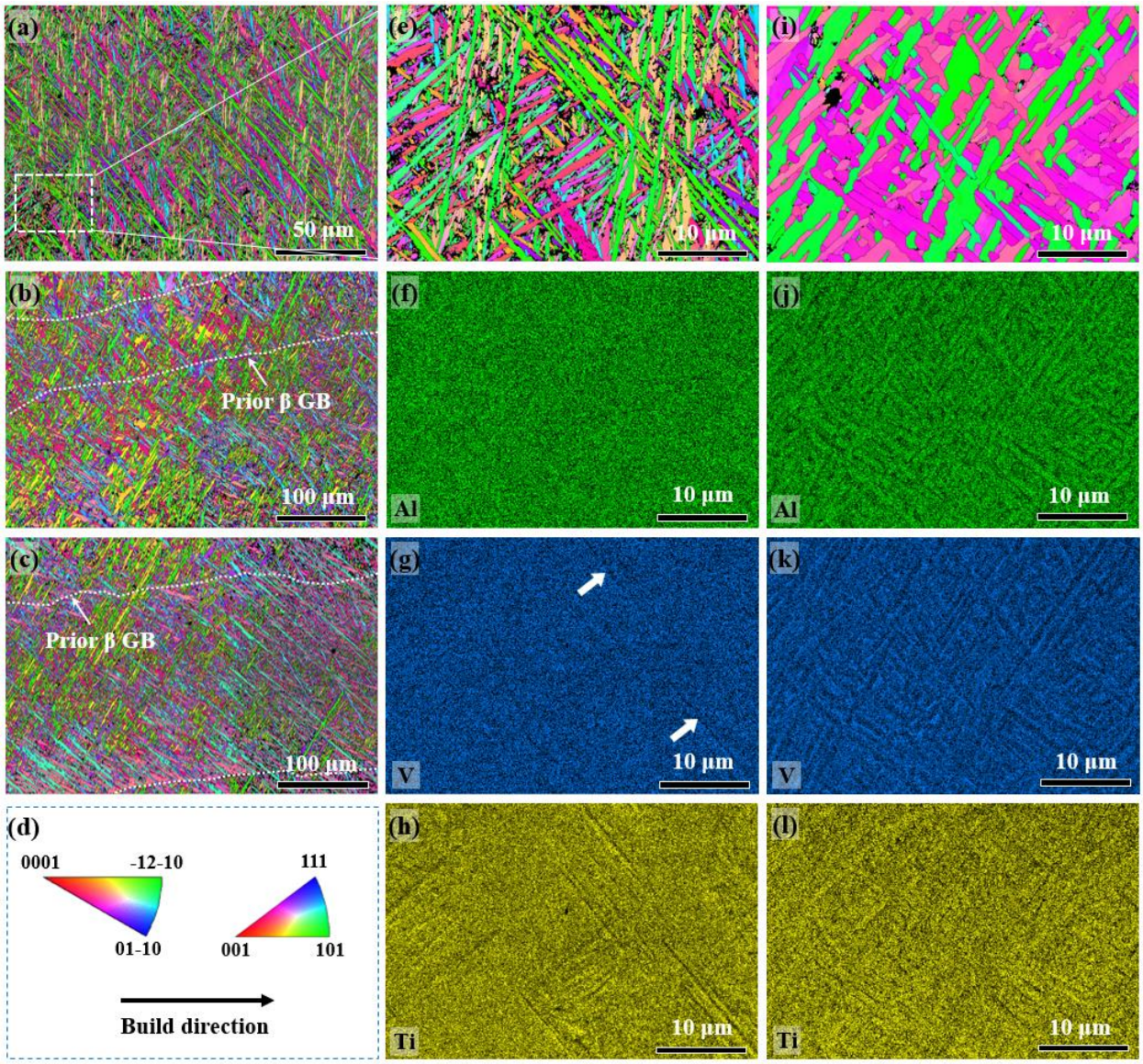

Fig. 8. (a, e) Inverse pole figure (IPF) map of the powder deposit. (e) is enlarged from the outlined position in (a). (b, i) IPF map of the wire deposit. (c) IPF map of the interface. (d) Color legend and build direction. (f, g, h) EDX mapping results for the position of (e). (j, k, l) EDX mapping results for the position of (i). Parent β grains were generated by using the parent grain analysis module in AZtecCrystal, and the parent β grain boundaries were outlined accordingly.

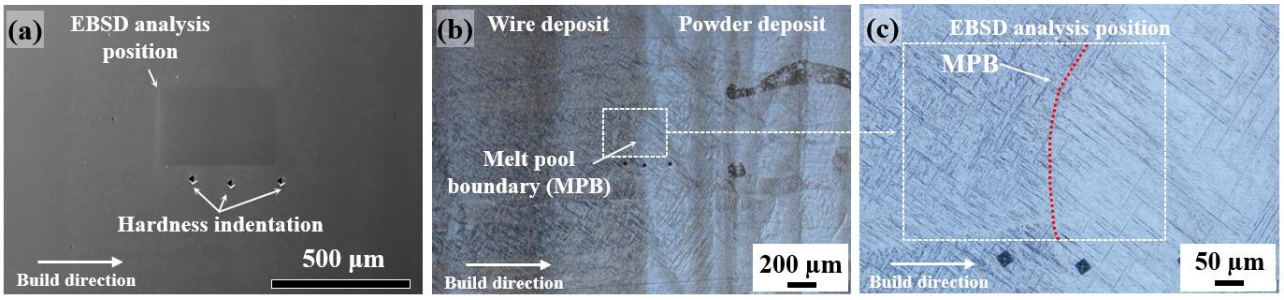

Fig. 9. (a) EBSD analysis position of the interface between the powder and wire deposits. (b, c) Enlarged images of the EBSD analysis position.

3.3. Mechanical behavior of the powder deposit, wire deposit, and interfacial samples

Representative engineering stress–strain curves are illustrated in Fig. 10(a). The tensile test results of the powder deposit, wire deposit, and different combinations are summarized in Fig. 10(b). Yield strength (YS), ultimate tensile strength (UTS), total elongation after fracture (El), and fracture position are tabulated in Table 3. As summarized in Table 3, no fracture occurred in the interfacial area, further implying the robust interface among the combinations of different deposits and forged substrates.

The forged Ti–6Al–4V demonstrates a good combination of strength and ductility. Its YS, UTS, and El are 905–973 MPa, 978–1035 MPa, and ~18%, respectively. The variation in strength is attributed to the microstructure difference in the different regions of the large forged component, as described in Section 2.1. The YS and UTS of all the deposited samples fall within the range of the forged substrate. An exception is the PD sample, which has an obviously higher UTS (~1079 MPa) due to the high cooling rate and fine α′ microstructure. The PD and WD samples show lower elongation than the forged substrate, which is quite common in additive-manufactured Ti–6Al–4V alloy, especially in the as-built state. Although the PD sample mainly comprises α′, it still contains a small amount of β phases (~0.16vol%, based on EBSD analysis). In comparison, the fraction of β phases in the WD sample is ~0.31vol%. Strain incompatibility between α′ and β will lead to stress concentration at the α′/β interface, resulting in premature failure and lower elongation [36]. Moreover, the PF and WF samples exhibit low elongation. Given that the gauge length of the tensile coupon comprises two sections with significantly different microstructures, deformation is mainly constrained within one side of the gauge length with lower strength [23], thereby causing lower elongation. For example, deformation occurs largely through the forged substrate in the PF sample instead of a uniform deformation within the whole gauge length, which can be verified from the cross-section of the fractured tensile coupon.

In this study, all analyses were conducted on materials in the as-built state without post heat treatment. Nevertheless, the performance of the different combinations of the deposits and forged substrate did meet the requirements of the corresponding Aerospace Material Specifications (AMS). As listed in Table 3, YS and UTS were considerably higher than the minimal value indicated in AMS 6932, whereas El was comparable to or even higher than the suggested value, such as the PW and WD samples. Notably, the YS and UTS of the PW sample are comparable to those of the WD, whereas its El is slightly lower. Owing to the higher strength of the powder deposit, plastic deformation is concentrated in the wire deposit region of the PW sample. Therefore, a lower elongation is obtained for the PW sample than for the WD sample. The different elongation is also demonstrated clearly from the stress–strain curves (Fig. 10(a)).

Herein, the microhardness distribution across the interface of the PW sample was measured and is depicted in Fig. 10(c). Corresponding to the finer microstructure, the powder deposit exhibits higher hardness ($HV_{0.3}$ (398.7 ± 9.7)) than the wire deposit ($HV_{0.3}$ (371.7 ± 7.9)). The difference in microhardness between the powder and wire deposits is only $HV_{0.3}$ ~27, implying the absence of an abrupt change in hardness distribution across the interface, which is favorable to the bonding of the different deposits. Considering the mechanical properties of the PW sample, the combination of $LAAM_p$ and $LAAM_w$ is applicable for the fabrication and repair of high-value titanium components.

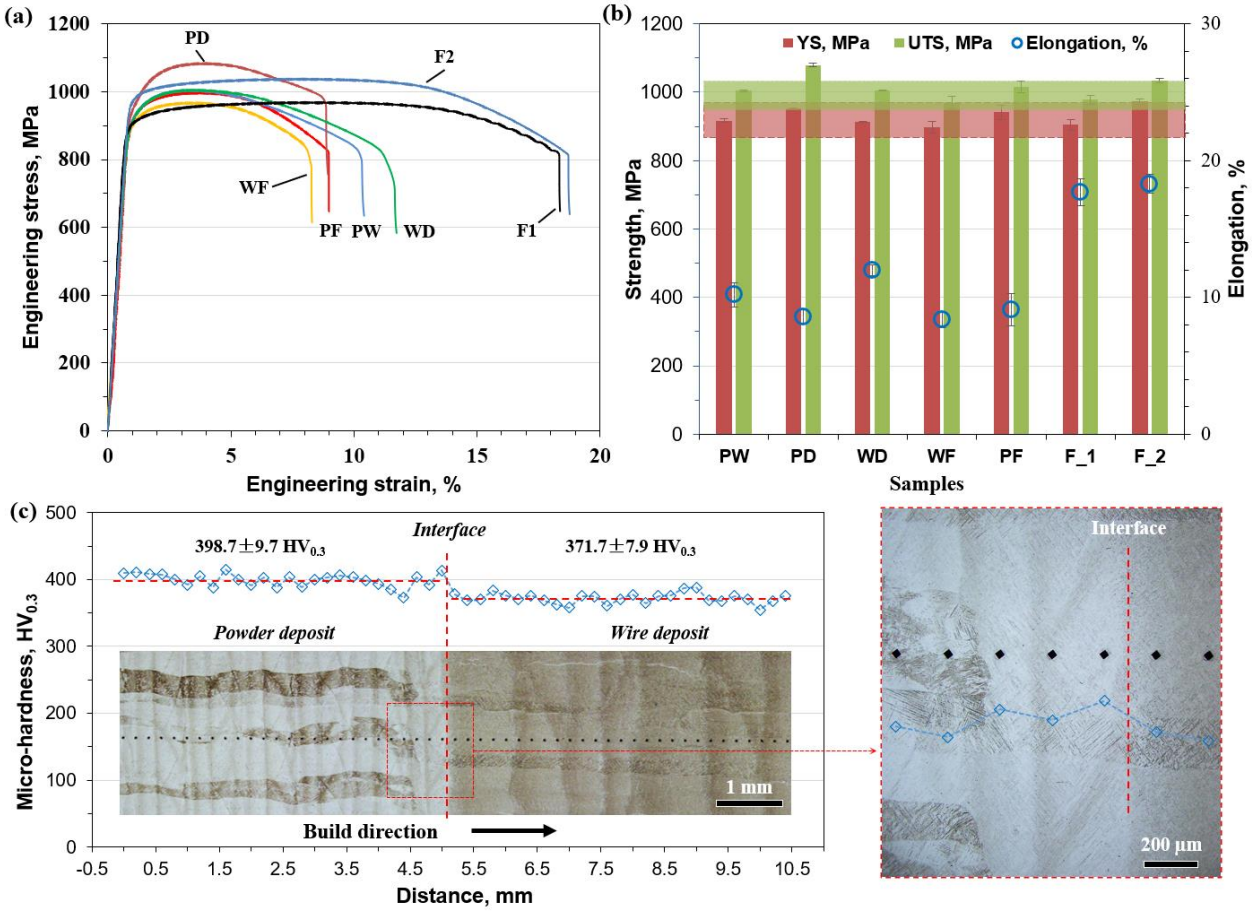

Fig. 10. (a) Representative engineering stress–strain curves. (b) Summary of the tensile test results (F_1: forged substrate far from the component surface (>30 mm); F_2: forged substrate near the component surface (<30 mm)). (c) Microhardness distribution across the interface of the PW sample.

Table 3. Summary of the tensile test results

Specimen	YS / MPa	UTS / MPa	El [a] / %	Fracture position
PF	941.6 ± 21.1	1015.5 ± 16.4	9.1 ± 1.2	Substrate
WF	897.3 ± 17.1	969.7 ± 18.3	8.4 ± 0.6	Wire deposit
PW	917.0 ± 5.1	1004.3 ± 1.9	10.2 ± 0.9	Wire deposit
PD	952.9 ± 0.9	1078.8 ± 3.9	8.4 ± 0.6	—
WD	913.4 ± 1.5	1005.4 ± 1.5	12 ± 0.4	—
F_1	904.6 ± 14.8	977.9 ± 13.9	17.7 ± 1.0	—

F_2	972.5 ± 9.1	1034.7 ± 6.1	18.3 ± 0.7	—
AMS 6932[b]	>792.9–827.4	>861.8–896.3	>6–10	—

Note: [a]Total fracture elongation. [b]Minimum requirements for Ti–6Al–4V (gd23) bars, forgings, and forging stock in accordance with the corresponding AMS.

3.4. Microstructure evolution after tensile deformation and fractograph analysis

Fig. 11 shows the cross-section morphologies of the fractured tensile coupons, wherein typical columnar epitaxial β grains are discernible. Fracture occurs at the forged substrate side of the PF tensile coupons, whereas the WF and PW tensile coupons fail at the wire deposit side, demonstrating the robust interfaces between the deposits and forged substrate as well as between the powder deposit and wire deposit. Given that the strength of the powder deposit is higher, fracture occurs at the forged substrate and wire deposit side in the PF and PW samples, respectively (Fig. 11(a) and (c)). Moreover, the forged substrate in the PF sample shows a coarser microstructure (Fig. 11(a)), corresponding to the materials extracted far from the surface of the large component. In comparison, the forged substrate side in the WF sample demonstrates a finer microstructure, implying higher strength (i.e., F_2 in Fig. 10(a)). Therefore, fracture occurs at the wire deposit side in the WF sample (Fig. 11(b)).

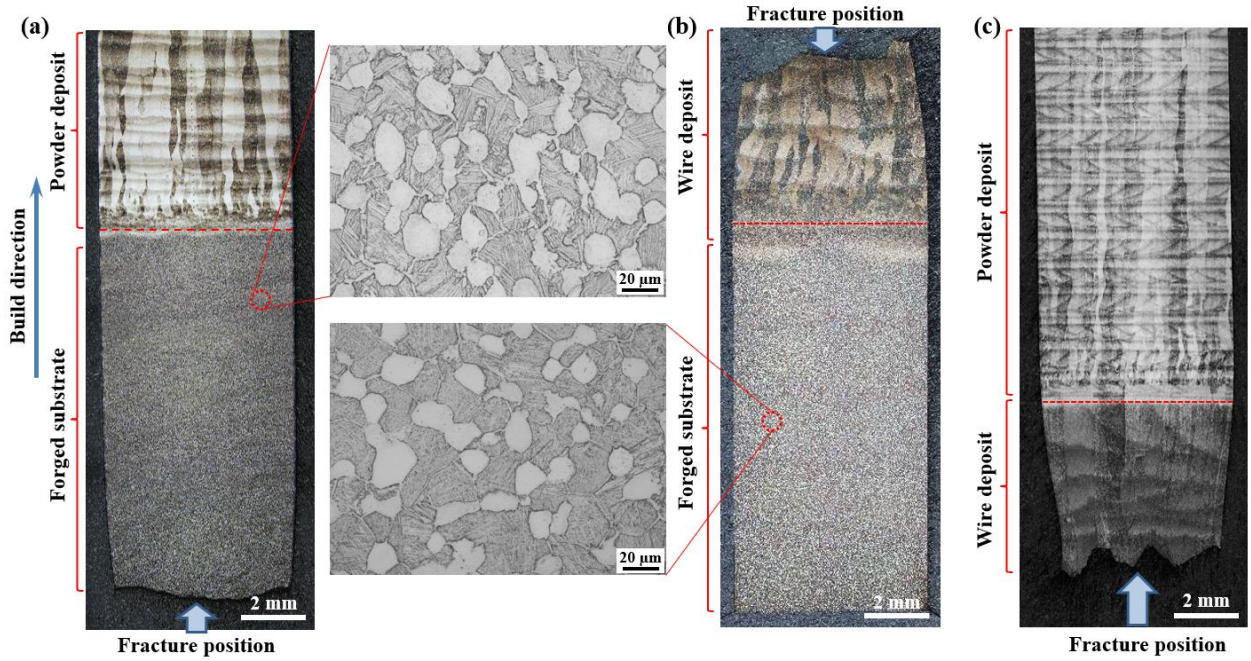

Fig. 11. (a) Cross-section of the fractured tensile coupon for the PF sample. (b) Cross-section of the fractured tensile coupon for the WF sample. (c) Cross-section of the fractured tensile coupon for the PW sample.

The PW sample was chosen to analyze microstructure evolution after the tensile test. As depicted in Fig. 11(c), obvious necking appears at the wire deposit side, implying severe deformation before fracture. An area with a distance of ~3.5 mm from the fracture position (Fig. 12(a)–(c)) was selected for EBSD analysis to ensure good data acquisition quality. Similar to the microstructure before tensile deformation, prior β grain boundaries (GBs), lamellar α, and Al segregation are all observed, as shown in Fig. 12(d)–(g). In comparison, the wire deposit shows considerably higher geometrically

necessary dislocation (GND) density after tensile fracture owing to dislocation multiplication during tensile deformation.

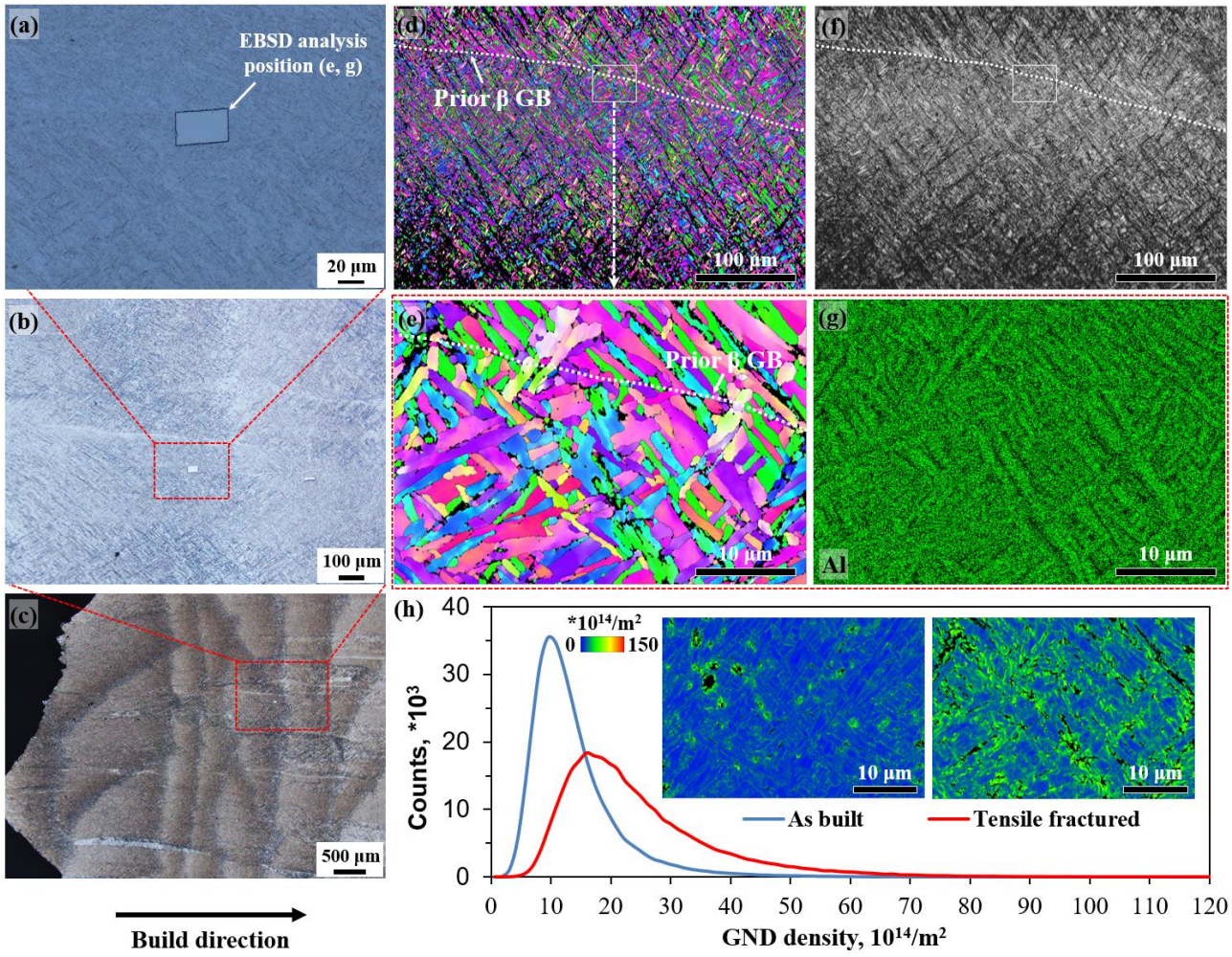

Fig. 12. (a–c) Illustration of the EBSD analysis position near the fractured position. (d, e) IPF map. (f) Band contrast map. (g) EDX map of Al for the same position in (e). (h) GND analysis results before and after tensile fracture (The analysis position of the as-built wire deposit to generate the GND results before tensile deformation is the same as that in Fig. 8(i). The acquisition step size is 0.06 μm). The IPF color legend is the same as that in Fig. 8(d). All the IPF maps are with respect to the build direction.

The fractographs of the PW, PF, and PD samples are shown in Fig. 13, representing the typical fracture morphologies of the wire deposit, forged substrate, and powder deposit, respectively. Generally, the fractographs of the alloys comprise fibrous, radial, and shear fracture zones corresponding to the initial fracture zone with slow and stable crack propagation, rapid crack growth zone, and final shear zone. However, the above-mentioned zones might not always appear depending on properties and test conditions [37]. The fractograph obtained in this study mainly comprises a central fibrous zone and surrounding shear fracture zone. Prevalent dimples suggest ductile fracture. Nonetheless, some cleavage-like features have appeared on the fractured surface of the powder and wire deposits (as indicated by arrows in Fig. 13(c), (g), and (i)). These fractures should be related to the columnar β grains growing along the build direction.

A few micropores are observed in the wire deposit (Fig. 13(b)). During $LAAM_w$, a small amount of argon gas might be entrapped into the deposit, forming micropores. In our study, the WD sample shows a good combination of strength and ductility, suggesting the insignificant influence of micropores on its tensile performance.

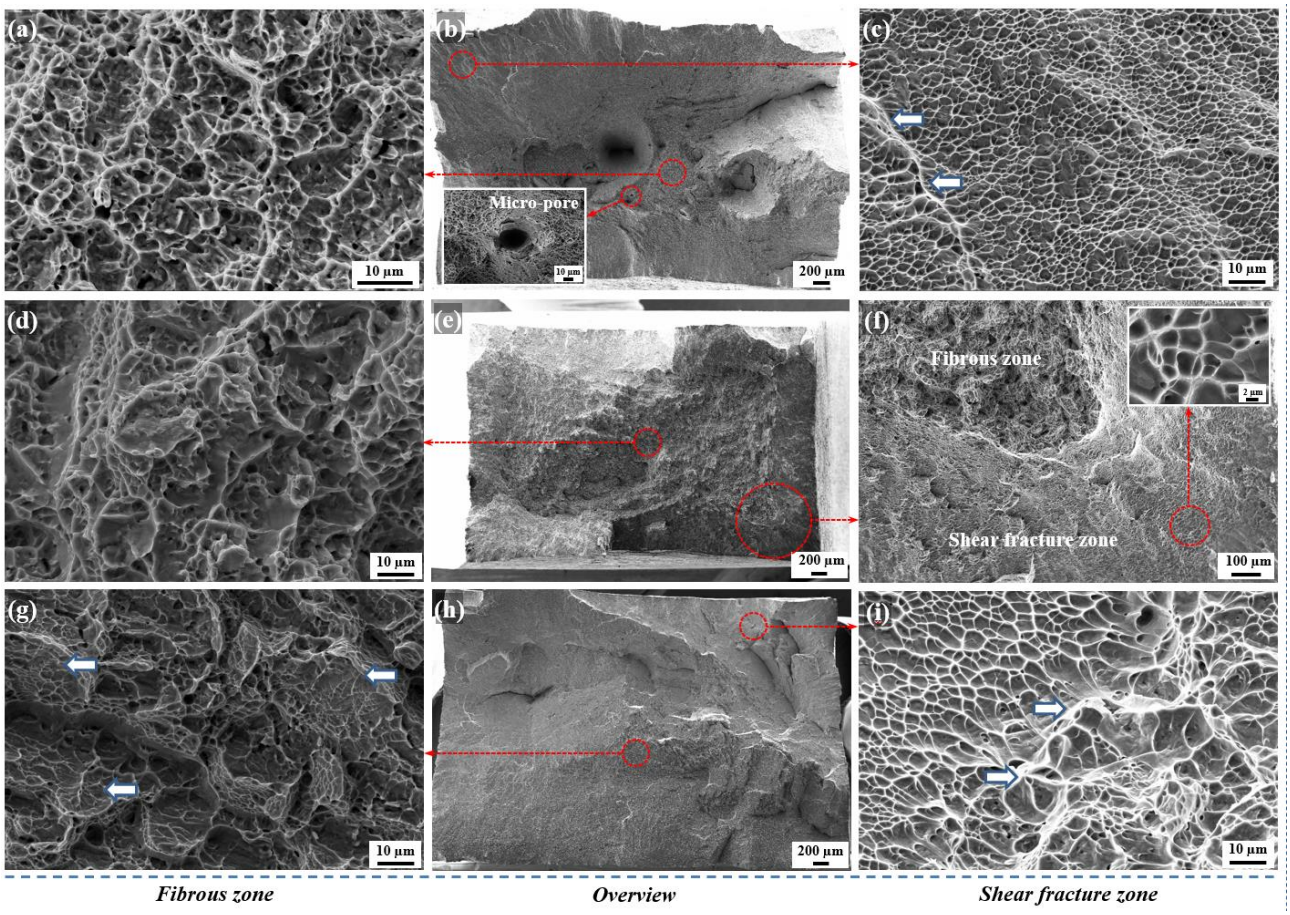

Fig. 13. (a–c) Fractograph of the PW sample (fractured at the wire deposit). (d–f) Fractograph of the PF sample (fractured at the forged substrate). (g–i) Fractograph of the PD sample.

4. Discussion

4.1. Effect of α′/α interphase boundaries on strengthening

As demonstrated in Section 3.2, the deposits mainly comprise lath-like α′ or α. The interfaces between laths play an important role in strengthening the Ti–6Al–4V alloy. The traditional Hall–Petch relationship was developed to correlate α′ or α lath thickness with yield strength. Herein, we used the formula proposed by Song *et al.* [38] to calculate yield strength:

$$\sigma_y = 750 + 179\, d^{-1/2},$$

where σ_y is the calculated yield strength (MPa), and d is the lath thickness of α′ or α (μm). The calculated results are summarized in Table 4. However, a gap ($\Delta\sigma$) exists between the calculated and experimental YS values. Although the Hall–Petch relationship is used to evaluate boundary strengthening, the nature of boundaries is always overlooked, and only grain size is considered. The effect of boundary type can be more important when it comes to titanium alloys.

Table 4. Summary of lath thickness and yield strength

Specimen	d / μm	Calculated YS, σ_y / MPa	Experimental YS / MPa	$\Delta\sigma$ / MPa
PD	1.1	921	953.2	32.2
WD	2.9	855	913.4	58.4

The transformation from parent β to α′ or α follows the Burgers orientation relationship, yielding 12 different α′ or α variants (i.e., variants A, B, …, L) and six types of boundaries between the variants (i.e., type I, II, …, VI). Under the condition of the random formation of the 12 variants, the length fraction of the boundaries should be 18.2% (type II), 36.4% (type III), 18.2% (type IV), 18.2% (type V), and 9.1% (type VI) [39]. Type II to type VI boundaries were outlined by using the special boundary module in AZtecCrystal 2.2, as demonstrated in Fig. 14(a)–(d). The length fraction and relative frequency of the misorientation degree are summarized in Fig. 14(e)–(g). In the powder deposit (Fig. 14(a) and (b)), most of the α′/α boundaries are type IV boundaries, whereas type II boundaries are prevalent in the wire deposit (Fig. 14(c) and (d)). The discrepancy between the measured boundary length fractions and the above values suggests that variant selection occurs in LAAM. The dominant type II and type IV boundaries are derived from the formation of two categories of self-accommodating variant clusters [39].

Lu *et al.* [40] reported the different variant selection phenomena in the columnar and equiaxed prior β grains of Ti–6Al–4V and Ti–6Al–2Sn–4Zr–2Mo α–β titanium processed through $LAAM_p$. In their study, the type IV boundary (<$\bar{1}0$ 5 5 $\bar{3}$>/63.26°) was prevalent in columnar β grains, whereas the type II boundary (<1 1 $\bar{2}$ 0>/60°) was common in equiaxed β grains, providing insights for understanding the effect of variant selection on mechanical properties. Type II boundaries, which always terminate on denser $\{10\bar{1}1\}$ planes, suggest lower boundary energy than the type IV boundaries terminating on $\{4\bar{1}\bar{3}0\}$. Therefore, type II boundaries are beneficial for the strengthening of Ti–6Al–4V alloy [40–41]. In our study, the prevalent type II boundaries in the wire deposit (42.1%) are expected to provide a more effective strengthening effect than the powder deposit. In other words, the $\Delta\sigma$ in Table 4 should be, at least partially, due to the omission of variation selection.

The higher fraction of type IV boundaries in the powder deposit (49.5%) should be related to the higher cooling rate during $LAAM_p$ than that during $LAAM_w$. Ma *et al.* [42] studied the effect of cooling rate on variant selection in Ti–6Al–4V processed by using $LAAM_p$ and attributed the beneficial effect of the cooling rate on the formation of type IV boundaries to higher residual stress. The boundary statistics results of the bottom section in Ref. [42] coincide well with those of the powder deposit in the present study. Moreover, the boundary length fraction (Fig. 14(e)) and relative frequency of the misorientation angle (Fig. 14(g)) of the powder deposit agree well with those

reported by Beladi *et al.* [43] on the variation selection of martensite in Ti–6Al–4V alloy. Similarly, Carrozza *et al.* [44] reported the same misorientation angle distribution in the as-built Ti–6Al–4V processed by using $LAAM_p$.

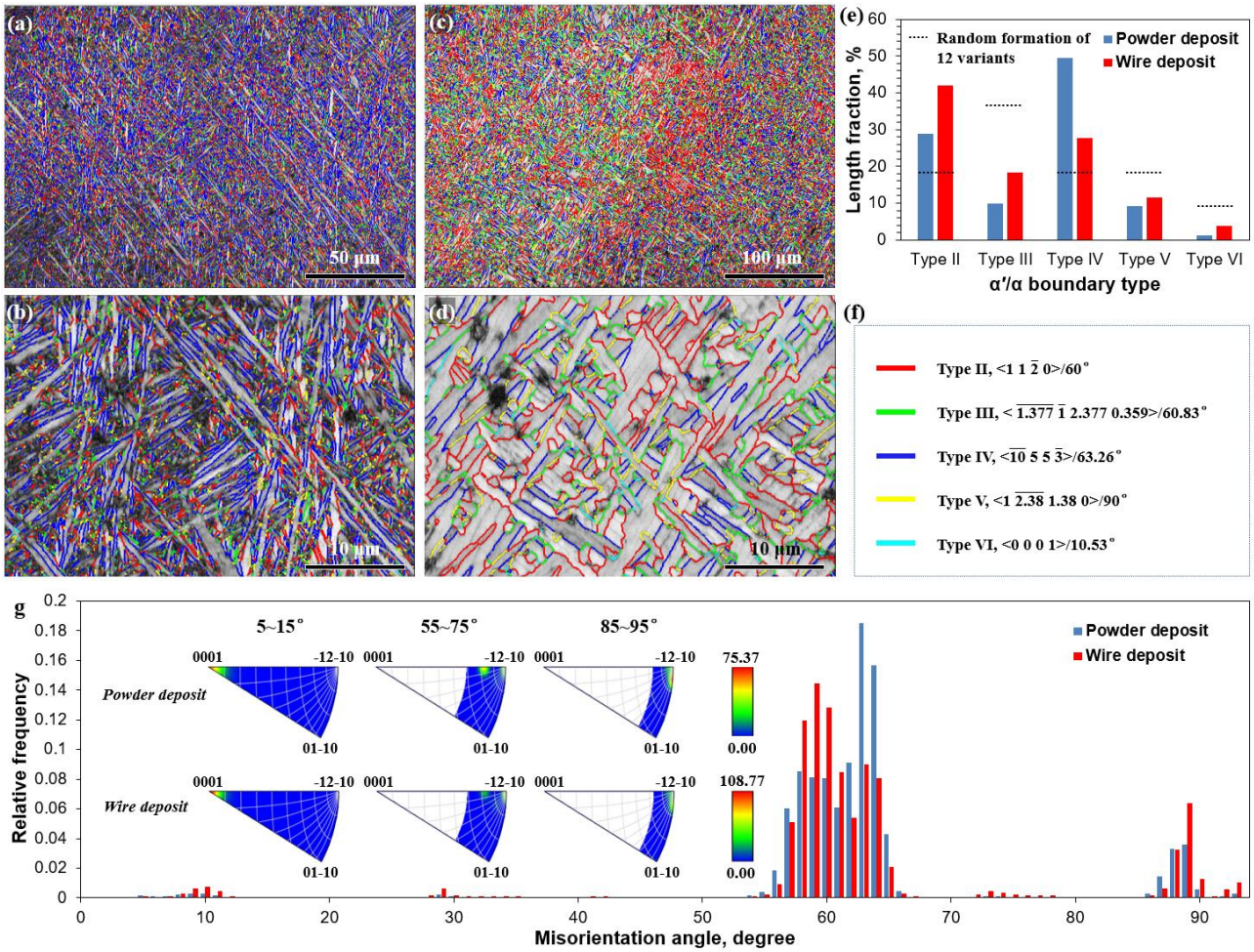

Fig. 14. Grain boundary (α′/α boundary) distribution on the band contrast maps of the (a, b) powder deposit and (c, d) wire deposit, (e) statistical result of the boundary length fraction, (f) legend for different boundaries, and (g) misorientation angle and axes.

4.2. Formation mechanism of the different microstructure characteristics

In this study, the powder deposit is characterized by acicular martensitic phases (α′) in the prior β grains (Figs. 7(b) and 8(e)). However, the α′ phases are partially decomposed, as inferred from the slight chemical segregation, particularly the distribution of V, indicated by the arrows in Fig. 8(g). Owing to the rapid cooling rate during laser-based AM processes, such as LAAM and SLM, a fully martensitic α′ is expected in the as-built state. However, it is not always true in the actual process because α′ is apt to decompose into α + β under the effect of the inherent heat treatment or *in-situ* heat treatment (IHT), which is closely related to heat input and the local thermal history. Therefore, a mixture of α′ and α + β or fully α + β microstructure is commonly observed in the as-built Ti–6Al–4V. For example, Zhao *et al.* [45] $LAAM_p$-processed Ti–6Al–4V by setting the linear energy density (the ratio of laser power to scan velocity) at 66.7 and 150 J/mm. The predominant α′ microstructure

presented in Ref. [45] is similar to that observed in the powder deposit in our study (Fig. 7(b)). Zhai *et al.* [22] observed prevalent α′ near the bottom of the deposit and α′ with α + β near the top of the deposit, wherein the microstructure variation is attributed to the decreasing cooling rate along the build direction. Zafari *et al.* [36,46] obtained a fully martensitic α′ microstructure in SLM-processed Ti–6Al–4V. However, it requires cautious heat input control and may only be attainable for processes involving pulsed lasers.

It is noteworthy that the decomposition of α′ is a diffusional process, the same as that in β → α transformation. Su *et al.* [47] conducted a systematic study on the decomposition of α′ by investigating microstructure evolution under different cooling rates and heat treatment procedures. Upon annealing, the characteristic α′ in the water quenching sample underwent decomposition accompanied by elemental partitioning and dislocation annihilation. Haubrich *et al.* [48] also revealed the effect of heat input on the decomposition of α′ by using different sets of SLM parameters with different IHT effects, as well as by using postannealing at different temperatures. In their study, some one- or two-dimensional V-enriched regions were observed in the vicinity of the α′ laths, which were thought to be related to the intrinsic defects in α′ and regarded as β-phase precursors.

Given that we used a continuous laser for $LAAM_p$, the same as that in most of the laser-based AM processes, obtaining a fully α′ microstructure is challenging. Hence, the partial decomposition of α′ is reasonable. The thin β film, derived from the decomposition of large primary α′, is the main cause of low elongation [46]. The common route to circumvent the detrimental effect of minor β phases (i.e., thin β film) is to achieve the well-developed equilibrium α + β lamellar structure via process modification or post heat treatment. Xu *et al.* [49] obtained a novel ultrafine lamellar α + β microstructure in SLM-processed Ti–6Al–4V with synergistic strength and ductility by utilizing the IHT effect to promote the decomposition of α′. Furthermore, an α + α′ duplex microstructure was found to be beneficial for enhancing the work hardening rate, which can be achieved by subtransus annealing followed by water quenching, as proposed by Formanoir *et al.* [50].

In contrast to the powder deposit, the wire deposit side demonstrates prevalent basket-weave α lamellae instead of acicular α′, as shown in Figs. 7(c) and 8(b) and (i). The difference is mainly attributed to the different cooling rates in $LAAM_p$ and $LAAM_w$. As listed in Table 1, $LAAM_w$ demonstrates higher heat input owing to its higher laser power and lower scanning velocity. By referring to the report from Farshidianfar *et al.* [51], a lower cooling rate is expected in $LAAM_w$. The lower cooling rate of $LAAM_w$ could retard martensitic transformation during deposition. In addition, the effect of IHT is promoted due to the larger heat input of $LAAM_w$, which eventually leads to an equilibrium basket-weave α/β lamellar microstructure.

4.3. Extended studies required to promote the application of $LAAM_p$ and $LAAM_w$

In this study, the combination of $LAAM_p$ and $LAAM_w$ was proposed to manufacture Ti–6Al–4V parts. With the integrated LAAM system prototype and optimized process parameters, manufacturing feasibility was preliminarily validated and supported by robust interfaces and comparable or superior tensile properties to the commercial alloys and AMS requirements. The underlying mechanisms of microstructure evolution and the correlation of microstructure–mechanical behavior were also revealed, laying a foundation for further property enhancement. Nonetheless, more extended studies are required to promote the synergistic application of $LAAM_p$ and $LAAM_w$.

Apart from static mechanical behavior, dynamic mechanical performance, such as the fatigue property of interfacial samples, should be evaluated, especially for application in the aerospace industry. In general, the fatigue performance of the as-built AM-processed materials is inferior to that of commercial materials. Posttreatment techniques, such as hot isostatic pressing, post heat treatment, shot peening, laser shock peening (LSP), and surface mechanical attrition treatment, are always employed to improve fatigue performance, as summarized in our previous review [2]. Instead of introducing an additional postprocessing step, adopting field-assisted AM [52] by integrating the auxiliary process (e.g., interlayer rolling or interlayer LSP) into LAAM is preferred to enhance fatigue properties by eliminating minimal defects (e.g., micropores), tailoring microstructures, and introducing a surface layer with compressive residual stress.

In summary, the idea of combining $LAAM_p$ and $LAAM_w$ to manufacture Ti–6Al–4V has been proven to be feasible. The outcomes presented in this study are helpful for promoting the advancement of LAAM with different forms of feedstocks to fulfill the requirements for deposition efficiency, dimensional accuracy, and excellent tensile properties without post heat treatment. At the same time, this study is expected to stimulate more follow-up studies on the fatigue property improvement of interfacial samples.

5. Conclusions

In this work, the combination of $LAAM_p$ and $LAAM_w$ was studied to fabricate Ti–6Al–4V parts. Manufacturing feasibility was explored from process optimization to microstructure characterization and mechanical property analysis. The main conclusions include the following:

(1) LoF defects in LAAM-processed Ti–6Al–4V can be eliminated by reducing material feed rates or increasing hatch distances (reducing overlap rates). In $LAAM_p$, a lower powder feed rate (1.37 g/min) with a laser power of 580 W was used to obtain defect-free deposits. In wire deposition, a slightly larger hatch distance (2.2 mm) was adopted to eliminate LoF defects. The interfaces among the powder/wire deposits and forged substrate obtained with the optimized parameters were proven to be robust. No interfacial defects were observed even

when the deposition was conducted directly on the as-built coarse surface of the powder or wire deposit.

(2) The LAAM-processed Ti–6Al–4V interfacial samples were characterized by epitaxial prior β grains growing across the deposition layers and interface of the powder/wire deposit. Acicular α′ martensitic phases precipitated in the powder deposit, and lamellar α phases were observed in the wire deposit. The α′ thickness (1.1 ± 0.3 μm) was considerably finer than the α lath thickness (2.9 ± 0.9 μm) owing to the higher cooling rate of $LAAM_p$. The type of α′/α interphase boundaries played an important role in strengthening tensile properties. The α′ in the powder deposit underwent partial decomposition due to the IHT effect.

(3) Different interfacial samples demonstrated comparable strength to the forged Ti–6Al–4V substrate (969.7–1015.5 MPa), whereas their elongation was lower (9.1%–10.2%). Their lower elongation was due to strain concentration on the gauge length side with lower strength. Although mechanical properties were evaluated with the samples in the as-built state, the tensile properties of the interfacial samples coincided well with AMS 6932.

(4) This work suggested the feasibility of using $LAAM_p$ and $LAAM_w$ to manufacture Ti–6Al–4V parts, add-on features, or repair high-value titanium components. This idea can also be extended to other material systems. Extended research should be conducted on the fatigue behavior of the interfacial samples to promote the applications of $LAAM_p$ and $LAAM_w$ in manufacturing components in the aerospace industry. Novel manufacturing routes for the fatigue property enhancement of the interfacial samples are expected to be stimulated in future work.

Acknowledgements

This work was supported by the Agency for Science, Technology and Research (A*Star), Republic of Singapore, under the Aerospace Consortium Cycle 12 “Characterization of the Effect of Wire and Powder Deposited Materials” (No. A1815a0078).

Conflicts of Interest

Guijun Bi is an editorial board member for this journal and was not involved in the editorial review or the decision to publish this article. The authors declare that they have no known competing financial interests or personal relationships that could have appeared to influence the work reported in this paper.

References

[1] G. Lütjering and J.C. Williams, *Titanium*, Springer, Berlin, 2007.

[2] C.L. Tan, F. Weng, S. Sui, Y. Chew, and G.J. Bi, Progress and perspectives in laser additive manufacturing of key aeroengine materials, *Int. J. Mach. Tools Manuf.*, 170(2021), art. No. 103804.

[3] S.H. Pan, G.C. Yao, Y.N. Cui, *et al.*, Additive manufacturing of tungsten, tungsten-based alloys, and tungsten matrix composites, *Tungsten*, 5(2023), No. 1, p. 1.

[4] H.J. Zong, N. Kang, Z.H. Qin, and M. El Mansori, A review on the multi-scaled structures and mechanical/thermal properties of tool steels fabricated by laser powder bed fusion additive manufacturing, *Int. J. Miner. Metall. Mater.*, 31(2024), No. 5, p. 1048.

[5] X.M. Cai, Y. Hou, W. Zhang, *et al.*, Mechanical behavior and response mechanism of porous metal structures manufactured by laser powder bed fusion under compressive loading, *Int. J. Miner. Metall. Mater.*, 31(2024), No. 4, p. 737.

[6] D.C. Kong, C.F. Dong, X.Q. Ni, *et al.*, Microstructure and mechanical properties of nickel-based superalloy fabricated by laser powder-bed fusion using recycled powders, *Int. J. Miner. Metall. Mater.*, 28(2021), No. 2, p. 266.

[7] S.Y. Liu and Y.C. Shin, Additive manufacturing of Ti6Al4V alloy: A review, *Mater. Des.*, 164(2019), art. No. 107552.

[8] T.L. Zhang and C.T. Liu, Design of titanium alloys by additive manufacturing: A critical review, *Adv. Powder Mater.*, 1(2022), No. 1, art. No. 100014.

[9] Y.W. Luo, M.Y. Wang, J.G. Tu, Y. Jiang, and S.Q. Jiao, Reduction of residual stress in porous Ti6Al4V by *in situ* double scanning during laser additive manufacturing, *Int. J. Miner. Metall. Mater.*, 28(2021), No. 11, p. 1844.

[10] L. Lan, R.Y. Xin, X.Y. Jin, S. Gao, and B. He, Influence of multiple laser shock peening treatments on the microstructure and mechanical properties of Ti–6Al–4V alloy fabricated by electron beam melting, *Int. J. Miner. Metall. Mater.*, 29(2022), No. 9, p. 1780.

[11] Singapore Institute of Manufacturing Technology (SIMTech), *Joint collaboration aims to enable mass industry adoption of LAAM technology*, SIMTech [2022-10-23]. https://www.a-star.edu.sg/simtech/news-events/SIMTech-Manufacturing-Matters/MM/research-spotlight/joint-collaboration-aims-to-enable-mass-industry-adoption-of-laam-technology

[12] Singapore Institute of Manufacturing Technology (SIMTech), *Laser aided additive manufacturing (LAAM)*, SIMTech [2022-10-23]. https://www.a-star.edu.sg/Collaborate/programmes-for-smes/tech-access/additive-manufacturing/laser-aided-additive-manufacturing-(laam)

[13] Singapore Institute of Manufacturing Technology (SIMTech), *Hybrid laser aided additive manufacturing technology platform*, SIMTech [2022-10-23]. https://www.a-star.edu.sg/simtech/news-events/SIMTech-Manufacturing-Matters/MM/research-spotlight/hybrid-laser-aided-additive-manufacturing-technology-platform

[14] F. Weng, Y.F. Liu, Y. Chew, L.L. Wang, B.Y. Lee, and G.J. Bi, Repair feasibility of SS416 stainless steel *via* laser aided additive manufacturing with SS410/Inconel625 powders, *IOP Conf. Ser. Mater. Sci. Eng.*, 744(2020), No. 1, art. No. 012031.

[15] Z.Q. Liu, R.X. Ma, G.J. Xu, W. Wang, and J. Liu, Laser additive manufacturing of bimetallic structure from Ti–6Al–4V to Ti–48Al–2Cr–2Nb via vanadium interlayer, *Mater. Lett.*, 263(2020), art. No. 127210.

[16] H. Paydas, A. Mertens, R. Carrus, J. Lecomte-Beckers, and J.T. Tchuindjang, Laser cladding as repair technology for Ti–6Al–4V alloy: Influence of building strategy on microstructure and hardness, *Mater. Des.*, 85(2015), p. 497.

[17] X.Z. Shi, S.Y. Ma, C.M. Liu, *et al.*, Selective laser melting-wire arc additive manufacturing hybrid fabrication of Ti–6Al–4V alloy: Microstructure and mechanical properties, *Mater. Sci. Eng. A*, 684(2017), p. 196.

[18] Q. Liu, Y.D. Wang, H. Zheng, *et al.*, Microstructure and mechanical properties of LMD–SLM hybrid forming Ti6Al4V alloy, *Mater. Sci. Eng. A*, 660(2016), p. 24.

[19] L. Yan, Y.T. Chen, and F. Liou, Additive manufacturing of functionally graded metallic materials using laser metal deposition, *Addit. Manuf.*, 31(2020), art. No. 100901.

[20] A. Reichardt, A.A. Shapiro, R. Otis, *et al.*, Advances in additive manufacturing of metal-based functionally graded materials, *Int. Mater. Rev.*, 66(2021), No. 1, p. 1.

[21] M. Rauch, J.Y. Hascoët, and M. Mallaiah, Repairing Ti–6Al–4V aeronautical components with DED additive manufacturing, *MATEC Web Conf.*, 321(2020), art. No. 03017.

[22] Y.W. Zhai, D.A. Lados, E.J. Brown, and G.N. Vigilante, Understanding the microstructure and mechanical properties of Ti–6Al–4V and Inconel 718 alloys manufactured by Laser Engineered Net Shaping, *Addit. Manuf.*, 27(2019), p. 334.

[23] Z. Zhao, J. Chen, H. Tan, X. Lin, and W.D. Huang, Evolution of plastic deformation and its effect on mechanical properties of laser additive repaired Ti64ELI titanium alloy, *Opt. Laser Technol.*, 92(2017), p. 36.

[24] Y.Y. Zhu, J. Li, X.J. Tian, H.M. Wang, and D. Liu, Microstructure and mechanical properties of hybrid fabricated Ti–6.5Al–3.5Mo–1.5Zr–0.3Si titanium alloy by laser additive manufacturing, *Mater. Sci. Eng. A*, 607(2014), p. 427.

[25] S.H. Mok, G.J. Bi, J. Folkes, and I. Pashby, Deposition of Ti–6Al–4V using a high power diode laser and wire, Part I: Investigation on the process characteristics, *Surf. Coat. Technol.*, 202(2008), No. 16, p. 3933.

[26] A. Ho, H. Zhao, J.W. Fellowes, F. Martina, A.E. Davis, and P.B. Prangnell, On the origin of microstructural banding in Ti–6Al4V wire-arc based high deposition rate additive manufacturing, *Acta Mater.*, 166(2019), p. 306.

[27] G.Y. Mi, Y. Xiang, C.M. Wang, L.D. Xiong, and Q.B. Ouyang, Microstructure and mechanical properties of SiC_p/Al composite fabricated by concurrent wire-powder feeding laser deposition, *J. Mater. Res. Technol.*, 22(2023), p. 66.

[28] F.Q. Li, Z.Z. Gao, L.Q. Li, and Y.B. Chen, Microstructural study of MMC layers produced by combining wire and coaxial WC powder feeding in laser direct metal deposition, *Opt. Laser Technol.*, 77(2016), p. 134.

[29] F. Wang, J. Mei, and X.H. Wu, Compositionally graded Ti6Al4V+TiC made by direct laser fabrication using powder and wire, *Mater. Des.*, 28(2007), No. 7, p. 2040.

[30] Y. Zhou and F.D. Ning, A feasibility study on directed energy deposition of SS 316L with coaxial wire-powder feeding, *Manuf. Lett.*, 33(2022), p. 686.

[31] W.U.H. Syed, A.J. Pinkerton, and L. Li, Combining wire and coaxial powder feeding in laser direct metal deposition for rapid prototyping, *Appl. Surf. Sci.*, 252(2006), No. 13, p. 4803.

[32] H.S. Lee, J.H. Yoon, C.H. Park, Y.G. Ko, D.H. Shin, and C.S. Lee, A study on diffusion bonding of superplastic Ti–6Al–4V ELI grade, *J. Mater. Process. Technol.*, 187-188(2007), p. 526.

[33] S. Sui, Y. Chew, F. Weng, C.L. Tan, Z.L. Du, and G.J. Bi, Achieving grain refinement and ultrahigh yield strength in laser aided additive manufacturing of Ti–6Al–4V alloy by trace Ni addition, *Virtual Phys. Prototyp.*, 16(2021), No. 4, p. 417.

[34] L.T. Liu, C.Y. Chen, R.X. Zhao, *et al.*, *In-situ* nitrogen strengthening of selective laser melted Ti6Al4V with superior mechanical performance, *Addit. Manuf.*, 46(2021), art. No. 102142.

[35] X.P. Tan, Y. Kok, W.Q. Toh, *et al.*, Revealing martensitic transformation and α/β interface evolution in electron beam melting three-dimensional-printed Ti–6Al–4V, *Sci. Rep.*, 6(2016), art. No. 26039.

[36] A. Zafari, M.R. Barati, and K. Xia, Controlling martensitic decomposition during selective laser melting to achieve best ductility in high strength Ti–6Al–4V, *Mater. Sci. Eng. A*, 744(2019), p. 445.

[37] R.W. Hertzberg, R.P. Vinci, and J.L. Hertzberg, *Deformation and Fracture Mechanics of Engineering Materials*, 5th ed., Wiley, New Jersey, 2012.

[38] T. Song, T. Dong, S.L. Lu, *et al.*, Simulation-informed laser metal powder deposition of Ti–6Al–4V with ultrafine α–β lamellar structures for desired tensile properties, *Addit. Manuf.*, 46(2021), art. No. 102139.

[39] S.C. Wang, M. Aindow, and M.J. Starink, Effect of self-accommodation on α/α boundary populations in pure titanium, *Acta Mater.*, 51(2003), No. 9, p. 2485.

[40] S.L. Lu, C.J. Todaro, Y.Y. Sun, T. Song, M. Brandt, and M. Qian, Variant selection in additively manufactured alpha-beta titanium alloys, *J. Mater. Sci. Technol.*, 113(2022), p. 14.

[41] S.L. Lu, J.H. Wang, Y.Y. Sun, T. Song, and M. Qian, Identification of unusual large zones of Category I triple-alpha-variant clusters in additively manufactured Ti–4Al–2V alloy, *Scripta Mater.*, 212(2022), art. No. 114578.

[42] J.K. Ma, Y.S. Zhang, J.J. Li, Z.J. Wang, and J.C. Wang, Variant selection within one β grain in laser solid formed Ti–6Al–4V alloys, *Mater. Charact.*, 185(2022), art. No. 111744.

[43] H. Beladi, Q. Chao, and G.S. Rohrer, Variant selection and intervariant crystallographic planes distribution in martensite in a Ti–6Al–4V alloy, *Acta Mater.*, 80(2014), p. 478.

[44] A. Carrozza, A. Aversa, F. Mazzucato, *et al.*, An investigation on the effect of different multi-step heat treatments on the microstructure, texture and mechanical properties of the DED-produced Ti–6Al–4V alloy, *Mater*. *Charact*., 189(2022), art. No. 111958.

[45] Z. Zhao, J. Chen, H. Tan, J.G. Tang, and X. Lin, *In situ* tailoring microstructure in laser solid formed titanium alloy for superior fatigue crack growth resistance, *Scripta Mater*., 174(2020), p. 53.

[46] A. Zafari and K. Xia, High Ductility in a fully martensitic microstructure: A paradox in a Ti alloy produced by selective laser melting, *Mater*. *Res*. *Lett*., 6(2018), No. 11, p. 627.

[47] J.L. Su, X.K. Ji, J. Liu, *et al.*, Revealing the decomposition mechanisms of dislocations and metastable α′ phase and their effects on mechanical properties in a Ti–6Al–4V alloy, *J*. *Mater*. *Sci*. *Technol*., 107(2022), p. 136.

[48] J. Haubrich, J. Gussone, P. Barriobero-Vila, *et al.*, The role of lattice defects, element partitioning and intrinsic heat effects on the microstructure in selective laser melted Ti–6Al–4V, *Acta Mater*., 167(2019), p. 136.

[49] W. Xu, M. Brandt, S. Sun, *et al.*, Additive manufacturing of strong and ductile Ti–6Al–4V by selective laser melting via *in situ* martensite decomposition, *Acta Mater*., 85(2015), p. 74.

[50] C. de Formanoir, G. Martin, F. Prima, *et al.*, Micromechanical behavior and thermal stability of a dual-phase α+α′ titanium alloy produced by additive manufacturing, *Acta Mater*., 162(2019), p. 149.

[51] M.H. Farshidianfar, A. Khajepour, and A.P. Gerlich, Effect of real-time cooling rate on microstructure in laser additive manufacturing, *J*. *Mater*. *Process*. *Technol*., 231(2016), p. 468.

[52] C.L. Tan, R.S. Li, J.L. Su, *et al.*, Review on field assisted metal additive manufacturing, *Int*. *J*. *Mach*. *Tools Manuf*., 189(2023), art. No. 104032.